CHEMICAL & BIOMEDICAL IMAGING

pubs.acs.org/ChemBioImaging

Article

Atomically Precise $Au_{50}Ag_2$-Based Contrast Agent for *In Vivo* Three-Dimensional Multispectral Photoacoustic Imaging

Ying An,[§] Xu Liu,[§] Yiran Li, Kun Wu, Hao Wang, Kaiyu Zhang, Jing Jia, Chaoyi Yang, Yunlong Chen, Yan Zhu,* and Huangxian Ju*

Cite This: https://doi.org/10.1021/cbmi.6c00115

Read Online

ACCESS | Metrics & More | Article Recommendations | Supporting Information

ABSTRACT: Multispectral photoacoustic (PA) imaging holds great potential in the clinical field. However, developing contrast agents with excellent properties remains a great challenge. Herein, we present an atomic-precision $Au_{50}Ag_2$-based nanoagent via dimerization and engineering of Au_{25} nanocluster. The dimerization achieves a PA spectral red-shift from 680 to 710 nm, a 5.1-fold amplification of PA sensitivity, and an enhancement of photothermal conversion efficiency from 33.9 to 47.1%, which is further increased to 54.7% upon hydrophobic-to-hydrophilic transfer. After targeted derivation, this nanoagent shows specific PA contrast in cell pellets and accurate spectral unmixing with endogenous chromophores (deoxyhemoglobin and oxyhemoglobin) in solid tumors, which leads to a precise protocol of three-dimensional multispectral PA imaging. This protocol can unveil spatiotemporal heterogeneities of tumor-associated events, such as blood oxygenation, blood volume, and nanoprobe delivery, providing a visualized understanding of nanoprobe−tumor interactions. This work establishes atomic-precision dimerization as a generalizable paradigm for engineering contrast agents, thus bridging the gap between nanocluster design and multispectral PA imaging applications.

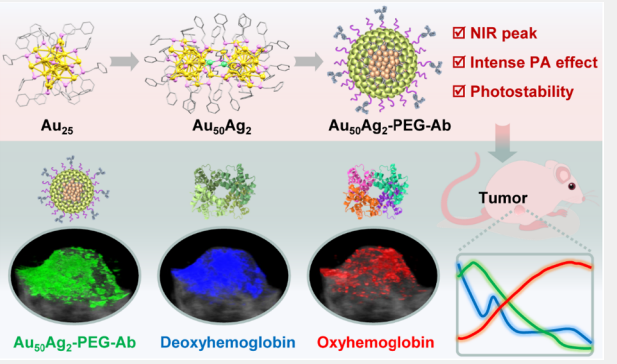

KEYWORDS: *gold nanocluster, $Au_{50}Ag_2$, photoacoustic agent, multispectral imaging, tumor*

INTRODUCTION

Multispectral photoacoustic (PA) imaging allows spectral differentiation of distinct chromophores (i.e., contrast agents) within target tissues with high resolution (down to several micrometers) and deep tissue penetration (from several millimeters to centimeters).[1,2] It can simultaneously reveal the three-dimensional (3D) physiological and molecular information with endogenous chromophores (such as hemoglobin) and exogenous contrast agents[3−6] and thus holds promising potential in preclinical research and clinical translation.[7,8] Ideal contrast agents to achieve these functions should meet the following photophysical requirements as much as possible: (1) characteristic near-infrared (NIR) absorption, (2) sufficiently intense PA effect, typically associated with high extinction coefficient, strong photothermal conversion, and low quantum yields, and (3) high photostability.[9−12] Gold nanocrystals (for example, gold nanorods) usually exhibit strong NIR absorption and efficient photothermal conversion owing to the localized surface plasmon resonance effect, enabling them to be widely used as PA nanoagents.[13,14] Although they possess spectral flexibility suitable for multispectral imaging, the relatively uncontrollable regulations of characteristic spectral shape and absorption wavelength and limited photostability remain tricky issues.[9,15] Therefore, there is an urgent need to develop new perspective nanoagents with excellent properties for advancing the practical applications of *in vivo* precise multispectral PA imaging.

Atomically precise metal nanoclusters (NCs), a new type of nanomaterial characterized by its atom packing structure and strong quantum confinement effects, display adjustable optical characteristics owing to their tunable electronic configurations.[16−20] Among metal NCs, Au NCs have been extensively applied in bioimaging due to their photoluminescence, intrinsic photostability, and biocompatibility.[21−24] They also exhibit optically excited acoustic vibrations,[25] and have been employed for *in vivo* PA imaging of metabolic processes.[26,27] However, the PA performance of Au NCs is greatly limited by the attenuated absorption characteristics in the NIR region, which hinders their application for multispectral PA imaging. Several strategies have been proposed to enhance the PA

Received: May 17, 2026
Revised: July 8, 2026
Accepted: July 8, 2026

Scheme 1. Schematic Illustration of Nanocluster Dimerization and Engineering for *In Vivo* 3D Multispectral PA Imaging[a]

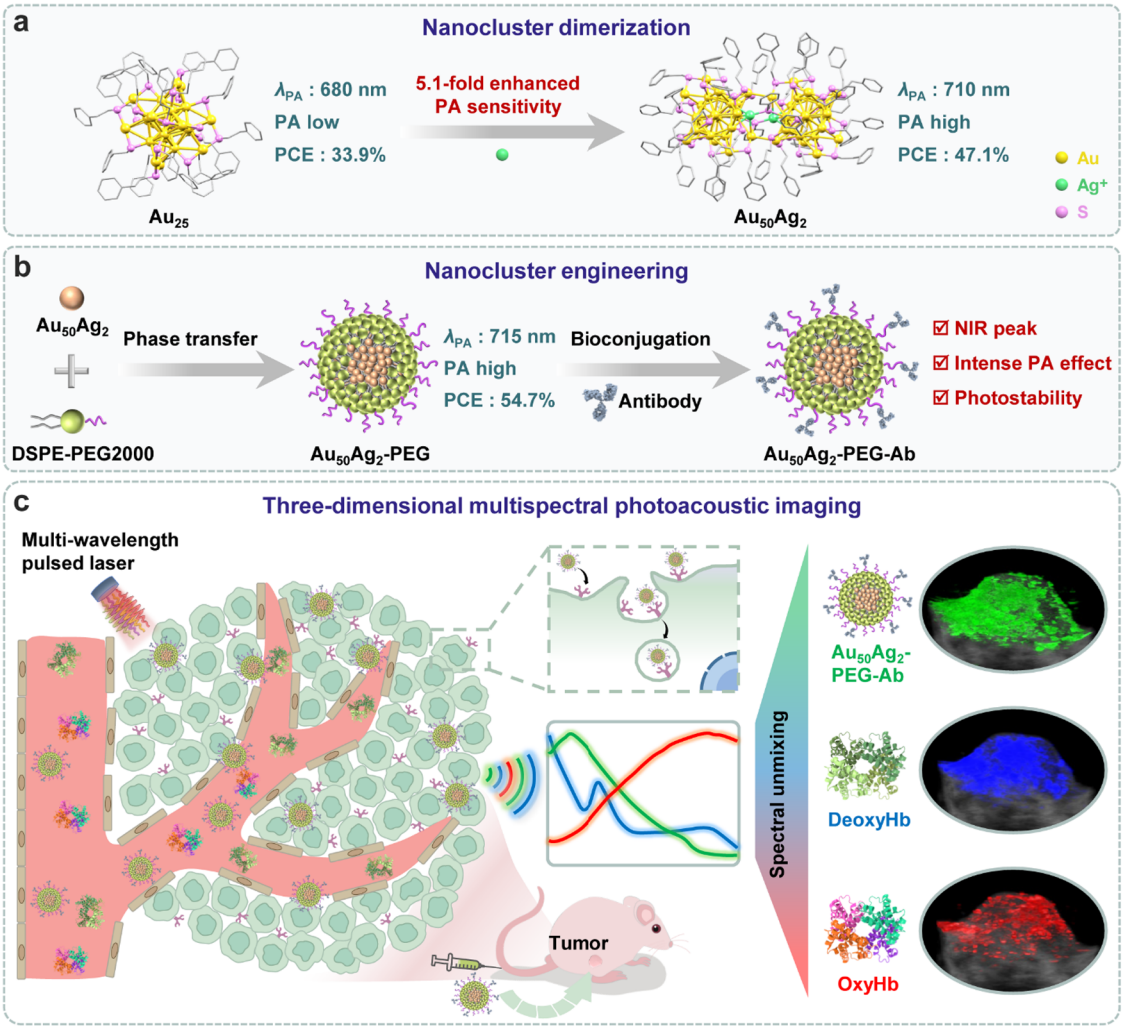

[a](a) Ag^+-triggered dimerization of Au_{25} into $Au_{50}Ag_2$ with PA and photothermal changes. (b) Nanocluster engineering from hydrophobic $Au_{50}Ag_2$ to hydrophilic $Au_{50}Ag_2$−PEG (phase transfer) and $Au_{50}Ag_2$−PEG-Ab nanoagent (bioconjugation with antibody). (c) Tumor-targeted delivery of $Au_{50}Ag_2$−PEG-Ab in tumor-bearing mice for 3D multispectral PA imaging of tumor-associated events (e.g., $Au_{50}Ag_2$−PEG-Ab, DeoxyHb, OxyHb).

intensity of Au NCs. For instance, Nieh et al. encapsulated $Au_{25}(SC_{16}H_{33})_{18}$ in lipid nanodisks to induce a 3-fold enhancement in PA signal by the aggregation of NCs.[28] Xie's group realized ethanol-triggered aggregation of $Au_{25}(Cys)_{18}$ NCs, which enhanced the PA intensity by ~3.3-fold.[29] However, these strategies retain the weak NIR absorption properties of $Au_{25}(SR)_{18}$ NCs, since the aggregating behavior does not alter the electronic structures of the original NCs, which leads to the limited enhancement of PA intensity, thus impeding the application of Au NCs in multispectral PA imaging. Therefore, it is necessary to seek novel solutions to substantially strengthen the PA intensity and improve the NIR absorption characteristics of Au NCs by structural modulations.

Recently, we synthesized a dimer $Au_{50}Ag_2(PET)_{36}$ NC (abbreviated as $Au_{50}Ag_2$) by assembling two $Au_{25}(PET)_{18}$ monomers (hereafter Au_{25}) bridged with two Ag^+.[30] The dimerization process resulted in the red-shift of the maximum absorption peak from 675 to 700 nm with an increase of molar extinction coefficient from 2.3×10^4 M^{-1} cm^{-1} to 9.6×10^4 M^{-1} cm^{-1}, as well as a significant decrease in photoluminescence intensity. Inspired by these findings, this work systematically investigates the photothermal conversion efficiency (PCE) and PA effects of the $Au_{50}Ag_2$ dimer and Au_{25} monomer and proposes an engineering strategy to facilitate hydrophobic-to-hydrophilic transfer and bioconjugation of $Au_{50}Ag_2$, which achieves the modulation of the PA sensitivity and PCE for constructing a novel high-performance PA contrast agent (Scheme 1a,b). Dimerization enhances the PA sensitivity by 5.1 folds, along with a distinct PA spectral red-shift from 680 to 710 nm and PCE change from 33.9 to 47.1%. The phase transfer can be realized by encapsulating $Au_{50}Ag_2$ with amphiphilic 1,2-distearoyl-*sn*-glycero-3-phosphoethanolamine-N-[methoxy (polyethylene glycol)-2000] (DSPE-PEG2000), which further red-shifts the characteristic PA peak and increases PCE. Using the tumor-specific antiepidermal growth factor receptor (EGFR) antibody (Ab) as an exemplary antibody conjugate, the developed $Au_{50}Ag_2$−PEG-Ab nanoagent exhibits superior PA contrast and accurate spectral unmixing with endogenous deoxyhemoglobin (DeoxyHb) and oxyhemoglobin (OxyHb) in tumor-bearing mice (Scheme 1c), indicating an excellent contrast agent and a precise protocol to achieve 3D multispectral PA imaging of a

https://doi.org/10.1021/cbmi.6c00115
Chem. Biomed. Imaging XXXX, XXX, XXX−XXX

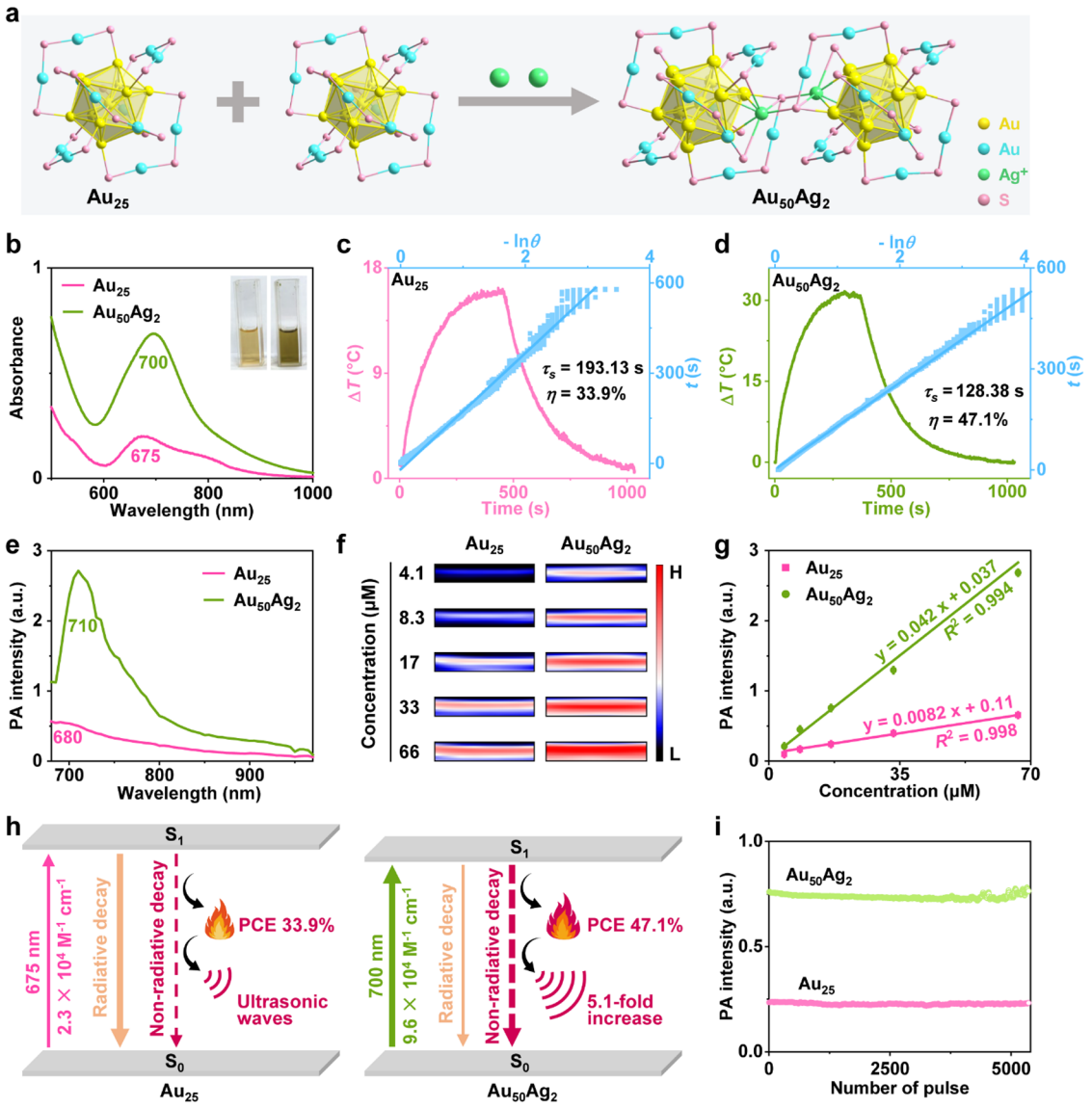

Figure 1. Optical properties of $Au_{50}Ag_2$ dimer versus Au_{25} monomer in the organic phase. (a) Schematic dimerization of two Au_{25} nanoclusters by two Ag^+ to $Au_{50}Ag_2$ dimer. C and H atoms are omitted for clarity. (b) Vis−NIR absorption spectra of Au_{25} and $Au_{50}Ag_2$ in THF (17 μM). The inset shows the photographs of Au_{25} (left) and $Au_{50}Ag_2$ (right). (c and d) Temperature changes of (c) Au_{25} and (d) $Au_{50}Ag_2$ in THF (17 μM) under 690 nm laser (1.0 W cm^{-2}), and plots of cooling time versus ln θ obtained during cooling. (e) PA spectra of Au_{25} and $Au_{50}Ag_2$ in THF (66 μM). (f) PA images of Au_{25} and $Au_{50}Ag_2$ in THF at indicated concentrations at 710 nm, and (g) plots of PA intensity versus the concentration. Data are presented as mean ± standard deviation (SD), n = 3. (h) Excited-state decay diagrams of Au_{25} and $Au_{50}Ag_2$. The molar extinction coefficients and radiative decay (i.e., photoluminescence) changes are from our previous report.[30] (i) PA intensity of Au_{25} and $Au_{50}Ag_2$ in THF (17 μM) during 5360 laser pulses at 710 nm.

tumor for unveiling the spatiotemporal heterogeneities of tumor-associated events.

RESULTS AND DISCUSSION

Optical Properties of $Au_{50}Ag_2$ in an Organic Phase

The dimeric $Au_{50}Ag_2$ nanocluster was formed by bridging two Au_{25} units with two Ag^+ in a "hand-in-hand" pattern (Figure 1a). The size of this atomically precise dimer was determined to be 1.3 nm by transmission electron microscopy (Figure S1). The spectral results indicated that $Au_{50}Ag_2$ showed NIR absorption peaking at 700 nm in both tetrahydrofuran (THF) and CH_2Cl_2, which red-shifted by 25 nm and was much stronger compared to Au_{25} monomer (Figures 1b and S2). Interestingly, the photothermal effect of the $Au_{50}Ag_2$ dimer was higher than that of the Au_{25} monomer. Specifically, the THF solution of $Au_{50}Ag_2$ showed a temperature increase (ΔT) of 31.7 °C after exposure to 690 nm irradiation, ~2-fold higher than that of Au_{25} (16.0 °C) (Figure 1c,d). Meanwhile, the temperature change of pure THF solvent was negligible upon exposure (Figure S3). Obviously, the temperature depended on both concentration and laser power density and approached a maximum value with increasing exposure time (Figure S4). From the plots of cooling time versus ln θ (a dimensionless parameter known as the driving force temperature), the PCEs (η) of $Au_{50}Ag_2$ and Au_{25} were determined to be 47.1 and 33.9%, respectively. The η value of $Au_{50}Ag_2$ in THF exceeded those of conventional atomically precise NCs except for several recently reported photothermal NCs[31−35] (Table S1). The high η value led to a much stronger PA peak of $Au_{50}Ag_2$ at 710

https://doi.org/10.1021/cbmi.6c00115
Chem. Biomed. Imaging XXXX, XXX, XXX−XXX

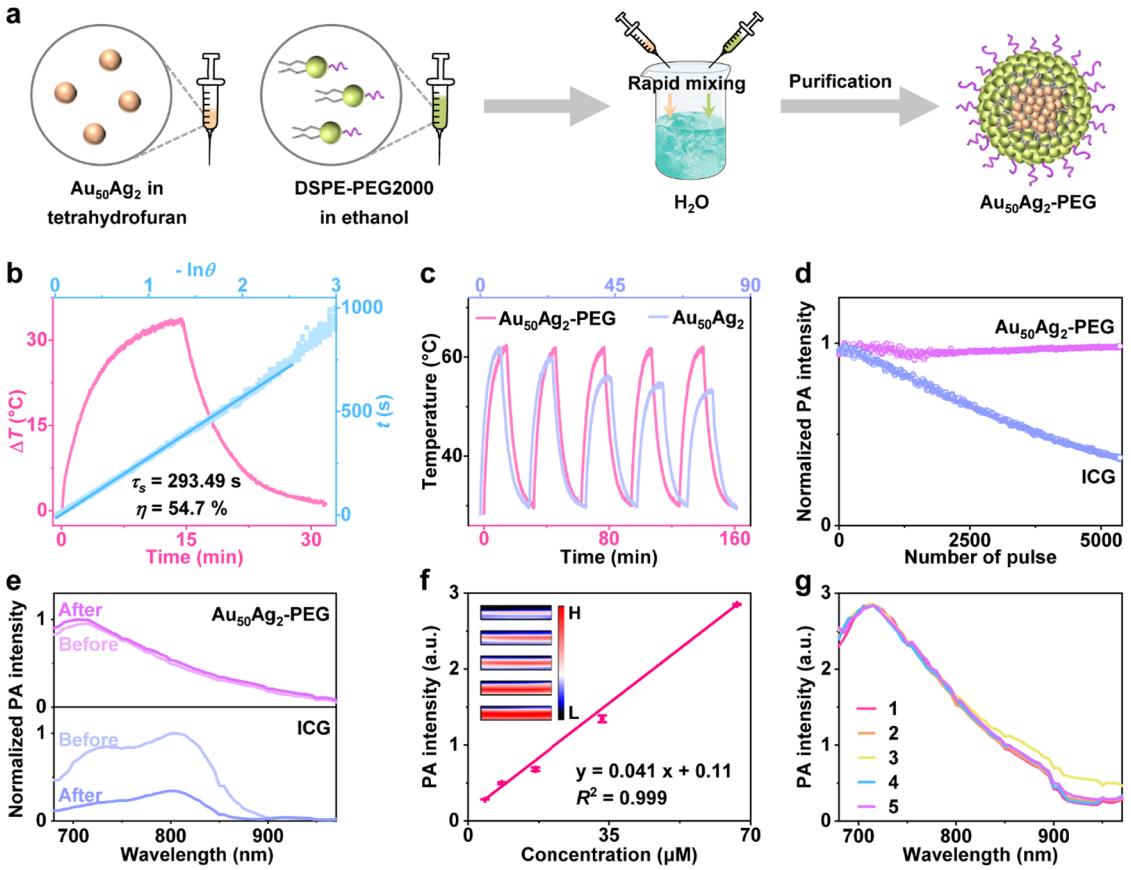

Figure 2. Optical properties of $Au_{50}Ag_2$–PEG nanoparticles in aqueous solution. (a) Schematic of the preparation of $Au_{50}Ag_2$–PEG. (b) Temperature change of $Au_{50}Ag_2$–PEG (17 μM) under a 690 nm laser (1.0 W cm^{-2}), and plot of cooling time versus ln θ obtained during cooling. (c) Photothermal stability of $Au_{50}Ag_2$–PEG in water (17 μM) and $Au_{50}Ag_2$ in THF (17 μM) during five cycles of laser irradiation at 690 nm (1.0 W cm^{-2}) and cooling. (d) PA intensity of $Au_{50}Ag_2$–PEG at 715 nm and ICG at 805 nm during 5360 laser pulses. (e) PA spectra of $Au_{50}Ag_2$–PEG and ICG before and after 5360 laser pulses. (f) Plot of PA intensity at 715 nm versus the concentration of $Au_{50}Ag_2$–PEG. The inset shows the corresponding PA images. Data are presented as mean ± SD (n = 3). (g) PA spectra of $Au_{50}Ag_2$–PEG (66 μM) in (1) H_2O, (2) PBS, (3) PBS2, (4) Ham's F12K medium, and (5) Ham's F12K medium with 10% FBS.

nm than that of Au_{25} at 680 nm in both THF and CH_2Cl_2 (Figures 1e and S5a). Remarkably, the strong and sharp PA peak of $Au_{50}Ag_2$, with its red-shift into the NIR region, rendered it highly suitable for *in vivo* PA applications. At 710 nm, both PA intensities of Au_{25} and $Au_{50}Ag_2$ were concentration-dependent (Figure 1f), indicating the potential for PA quantitative analysis. From the plots of PA intensity versus concentration, the slope for $Au_{50}Ag_2$, as its PA sensitivity, was ~5.1-fold higher than that for Au_{25} (Figure 1g), demonstrating a superior PA effect of $Au_{50}Ag_2$. Furthermore, at the same Au mass concentration, $Au_{50}Ag_2$ showed a ~2.5-fold higher sensitivity (Figure S5b), confirming that the enhancement originates primarily from the dimeric architecture rather than from a mere increase in gold content. Overall, the dimerization of Au_{25} not only red-shifted the absorption peak with enhanced intensity and reduced photoluminescence but also improved the photothermal conversion and intensified the PA peak along with a red-shift, indicating attenuated radiative decay and enhanced nonradiative decay (Figure 1h). Additionally, both Au_{25} and $Au_{50}Ag_2$ showed insignificant PA signal change during 5360 laser pulses (Figure 1i), demonstrating the intrinsic photostability of Au NCs.

Optical Properties of $Au_{50}Ag_2$–PEG in Aqueous Solution

Water-soluble $Au_{50}Ag_2$–PEG nanoparticles were prepared by mixing hydrophobic $Au_{50}Ag_2$ (dissolved in tetrahydrofuran) with amphiphilic DSPE-PEG2000 (dissolved in ethanol) in water under vigorous stirring (Figure 2a). This approach circumvented the structural alteration of metal NCs, thereby preserving the intrinsic spectral characteristics inherited from the organic phase while enabling facile surface functionalization[28,36–38] for advancing PA bioimaging applications. The mass ratio of $Au_{50}Ag_2$ to DSPE-PEG2000 was optimized to be 4.0/10.0 (mg) (Figures S6–S10), at which $Au_{50}Ag_2$–PEG exhibited a multicore structure with a hydrodynamic diameter of ~81.6 nm and the most uniform size distribution (i.e., minimal polydispersity index), with almost unchanged absorption and PA features compared to $Au_{50}Ag_2$ with sufficient intensities, and excellent freeze-drying and redissolving stability for long-term storage. Interestingly, this phase transfer process resulted in a slight red-shift of the $Au_{50}Ag_2$ PA peak from 710 to 715 nm. In addition, an encapsulation efficiency of ~100% could be achieved due to the strong hydrophobicity of $Au_{50}Ag_2$ (Figure S11). The photothermal results indicated that the $Au_{50}Ag_2$–PEG solution exhibited greater temperature increase (33.8 °C) than $Au_{50}Ag_2$ in THF (31.7 °C) upon 690 nm irradiation (Figure 2b). From the negligible temperature variation of pure water (Figure S12), the η value of the $Au_{50}Ag_2$–PEG solution (17 μM) was calculated to be 54.7%, higher than 47.1% for $Au_{50}Ag_2$ in THF with the same concentration. The η value of $Au_{50}Ag_2$–PEG

https://doi.org/10.1021/cbmi.6c00115
Chem. Biomed. Imaging XXXX, XXX, XXX–XXX

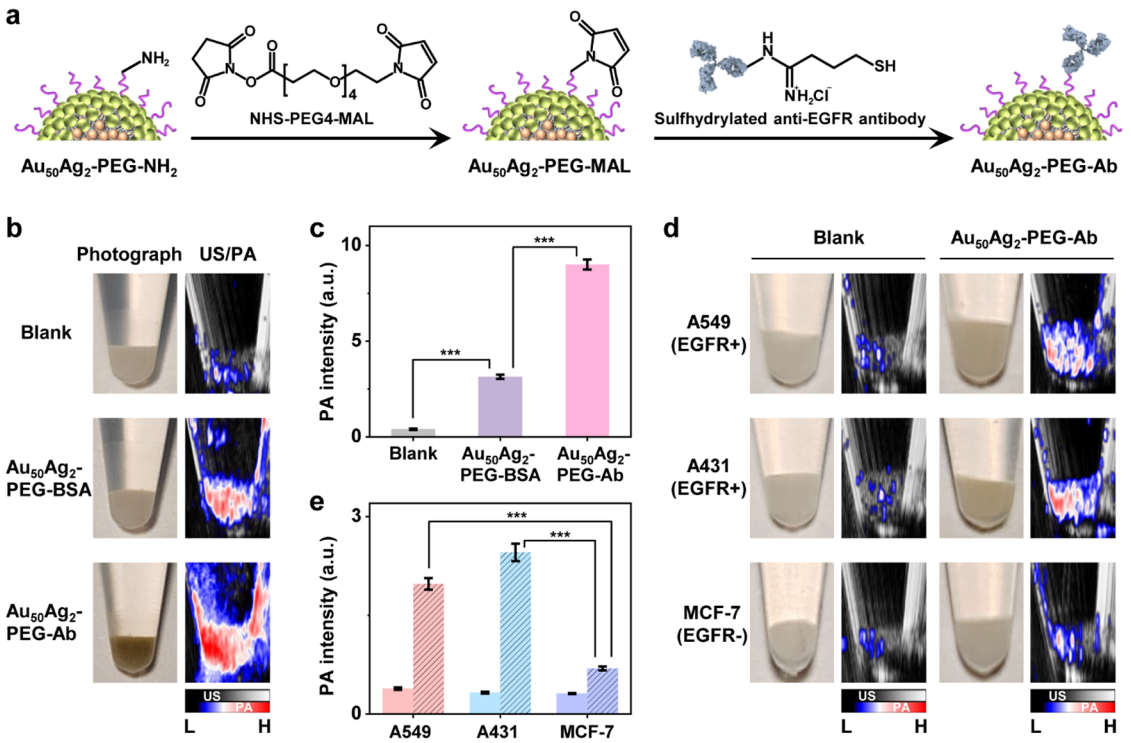

Figure 3. Construction of $Au_{50}Ag_2$−PEG-Ab for cell-targeted PA imaging. (a) Schematic of preparation of $Au_{50}Ag_2$−PEG-Ab. (b and c) Photographs and ultrasonic (US)/PA images of A549 cell pellets after incubation with $Au_{50}Ag_2$−PEG-BSA or $Au_{50}Ag_2$−PEG-Ab (17 μM), and PA intensity. ***$p < 0.00001$. (d and e) Photographs and US/PA images of A549, A431 and MCF-7 cell pellets after incubation with $Au_{50}Ag_2$−PEG-Ab (3.3 μM), and PA intensity. ***$p < 0.00003$. Blank: cell pellets without any treatment. Data are presented as mean ± SD ($n = 3$).

was also higher than those of previous NC-based photothermal agents in aqueous solutions except for the recently reported photothermal nanomachines[36] (Table S2). Particularly, $Au_{50}Ag_2$−PEG exhibited better photothermal stability compared to $Au_{50}Ag_2$ in THF (Figures 2c and S13), which might be attributed to the protection of DSPE-PEG2000 layers. Using classical PA contrast agent indocyanine green (ICG) as a control, the PA stability of $Au_{50}Ag_2$−PEG was examined by monitoring its PA response under 5360 laser pulses. $Au_{50}Ag_2$−PEG displayed relatively stable PA spectral characteristics and intensities at different concentrations, while ICG exhibited a drastic decrease of PA intensity along with the change of PA profile (Figures 2d,e and S14). The superior stability of $Au_{50}Ag_2$−PEG was further proved by its vis−NIR absorption spectra, which were almost identical before and after laser pulses, contrary to a 24-fold decrease in ICG absorbance at 780 nm (Figure S15). In addition, the PA stability of commercial gold nanorods (Au NRs, 80 nm × 20 nm) was also evaluated (Figure S16). The PA signal exhibited significant decay, accompanied by the disappearance of the PA peak at 825 nm. Absorption spectra revealed a marked decrease in intensity at 815 nm and an increase at 520 nm (derived from gold nanospheres), indicating poor photostability of the Au NRs due to fragmentation and shape transformation under nanosecond-pulse irradiation.[39−41] Surprisingly, the phase transfer did not change the positive concentration-dependent PA tendency or the PA sensitivity of $Au_{50}Ag_2$−PEG in aqueous solution relative to those of $Au_{50}Ag_2$ in THF (Figure 2f), implying the possibility of $Au_{50}Ag_2$−PEG for quantitative analysis applications. In addition, $Au_{50}Ag_2$−PEG showed nearly identical PA spectra and intensities in different physiological media (Figure 2g) and exhibited remarkable storage stability (Figure S17) and negligible change of PA intensity during 5360 laser pulses at 715 nm (Figure S18), suggesting its superiority for biological PA application. Overall, water-soluble $Au_{50}Ag_2$−PEG exhibited improved photothermal conversion and photothermal stability compared to $Au_{50}Ag_2$, and the superior PA stability against laser irradiation and long-term storage across different physiological media, which were conducive to accurate multispectral PA imaging in biological systems for practical applications.

Construction of an $Au_{50}Ag_2$−PEG-Ab Nanoagent for Cellular PA Imaging

To achieve targeted PA imaging, $Au_{50}Ag_2$−PEG-NH_2 was first synthesized by rapidly mixing the THF dispersion of $Au_{50}Ag_2$ with the ethanol solution of DSPE-PEG2000-NH_2 and DSPE-PEG2000, which also showed an encapsulation efficiency of ∼100% (Figure S19). Then, $Au_{50}Ag_2$−PEG-NH_2 was reacted with a heterobifunctional linker NHS-PEG4-MAL to obtain maleimide-functionalized $Au_{50}Ag_2$−PEG-MAL for covalently conjugating anti-EGFR antibody via maleimide−thiol click chemistry (Figure 3a). Compared to $Au_{50}Ag_2$−PEG, $Au_{50}Ag_2$−PEG-NH_2 showed a similar hydrodynamic diameter and better dispersity in H_2O due to the presence of the $-NH_2$ group, which also attenuated the negative ζ-potential (Figures S7f and S20a,b). Nevertheless, the conjugation of protein molecules to $Au_{50}Ag_2$−PEG-NH_2 decreased the ζ-potential and increased the hydrodynamic diameter of $Au_{50}Ag_2$−PEG-Ab to ∼98.2 nm and that of $Au_{50}Ag_2$−PEG-BSA to ∼93.8 nm (Figure S20a,c,d). Under physiological conditions (i.e., PBS), although the hydrodynamic diameter of $Au_{50}Ag_2$−PEG-Ab (∼110.2 nm) and $Au_{50}Ag_2$−PEG-BSA (∼104.2 nm) slightly increased (Figure S20e,f), the intrinsic PA spectral profile and PA sensitivity of $Au_{50}Ag_2$−PEG-Ab remained unchanged (Figure

https://doi.org/10.1021/cbmi.6c00115
Chem. Biomed. Imaging XXXX, XXX, XXX−XXX

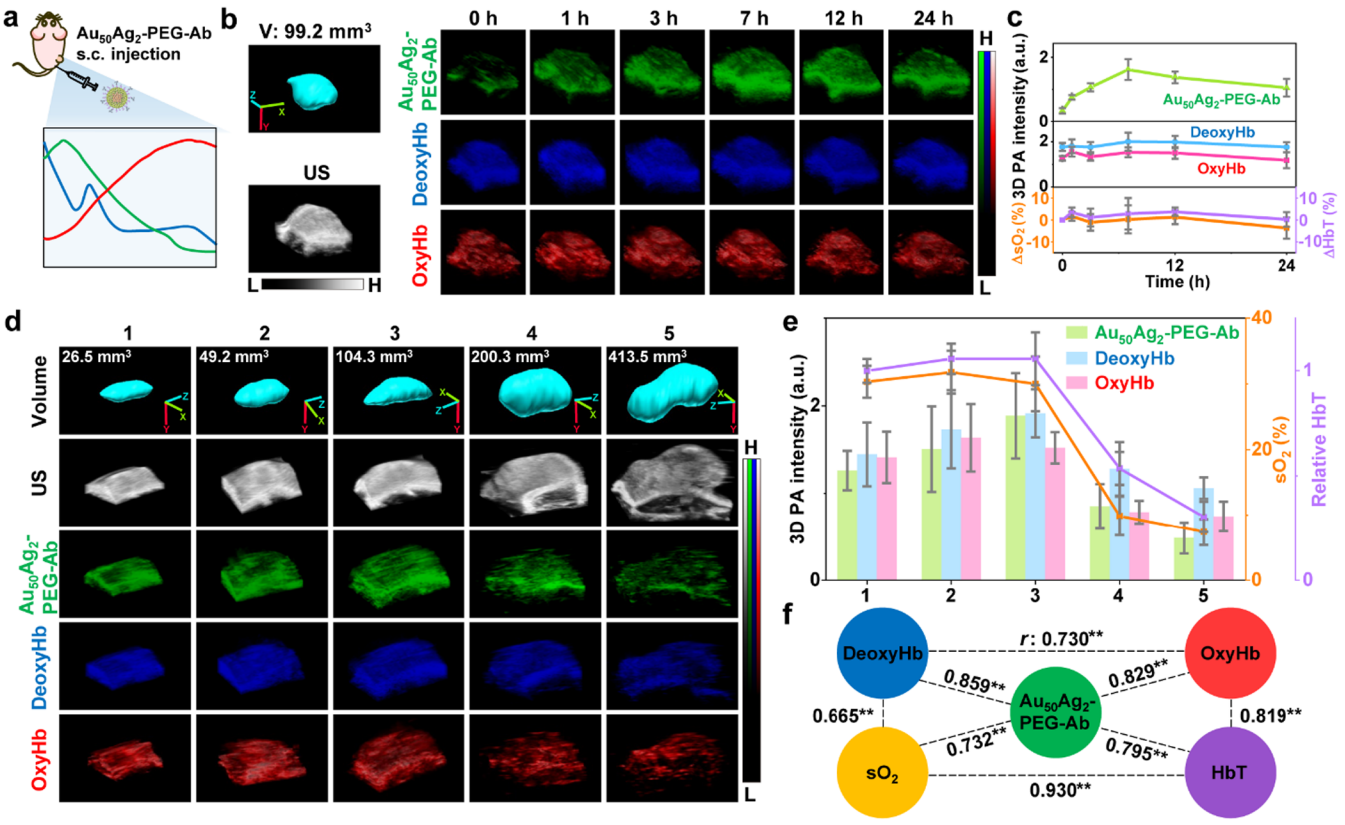

Figure 4. *In vivo* 3D multispectral PA imaging of three components in tumors upon s.c. injection. (a) PA spectra of $Au_{50}Ag_2$−PEG-Ab (green), DeoxyHb (blue), and OxyHb (red) in the A549 tumor after the s.c. injection of $Au_{50}Ag_2$−PEG-Ab. (b) Representative 3D volume and US image, and multispectral PA images of tumor before (0 h) and after the injection of $Au_{50}Ag_2$−PEG-Ab (17 μM, 100 μL) for different times. (c) 3D PA intensity of $Au_{50}Ag_2$−PEG-Ab, DeoxyHb, and OxyHb, and the relative changes of sO_2 and HbT at different times. Data are presented as mean ± SD (n = 3 mice). (d) Representative 3D volumes and US images, and multispectral PA images of different tumors after the s.c. injection of $Au_{50}Ag_2$−PEG-Ab (17 μM, 100 μL) for 7 h. (e) 3D PA intensity of $Au_{50}Ag_2$−PEG-Ab, DeoxyHb and OxyHb, sO_2 and HbT in different tumors. Data are presented as mean ± SD (n = 4 mice). (f) Correlation analysis among the PA signals of $Au_{50}Ag_2$−PEG-Ab, DeoxyHb, and OxyHb, and the values of sO_2 and HbT in 20 mice. $^{**}p \leq 0.001$.

S21), suggesting its physiological availability. Using human lung adenocarcinoma cell line A549 with high EGFR expression[42−44] as a model, we found that $Au_{50}Ag_2$−PEG-Ab exhibited negligible cytotoxicity, similar to $Au_{50}Ag_2$−PEG-BSA (Figure S22). In addition, the efficient cellular uptake and lysosomal accumulation of $Au_{50}Ag_2$−PEG-Ab in A549 cells were demonstrated by fluorescence imaging with Cy5.5-labeled $Au_{50}Ag_2$−PEG-Ab ($Au_{50}Ag_2$−PEG-Ab/Cy5.5) (Figures S23−S25). As for PA imaging, after incubating A549 cells with different concentrations of $Au_{50}Ag_2$−PEG-Ab, the PA signal of the resulting cell pellets showed a linear increase (R^2 = 0.991) (Figure S26), indicating the feasibility of $Au_{50}Ag_2$−PEG-Ab for cellular PA quantitation. Using $Au_{50}Ag_2$−PEG-BSA as a nontargeted control agent, the A549 cell pellet treated with either $Au_{50}Ag_2$−PEG-Ab or $Au_{50}Ag_2$−PEG-BSA showed a significantly higher PA signal than the blank, while the PA intensity of the $Au_{50}Ag_2$−PEG-Ab group was much stronger (Figure 3b,c), indicating the benefit of active targeting. This superiority was further validated by examining the PA imaging signals from human epidermoid carcinoma cell line A431 with high EGFR expression[45,46] and human breast cancer cell line MCF-7 with low EGFR expression.[45,47] As expected, MCF-7 cell pellets exhibited weak PA intensity, while the PA signal of A431 cell pellets was significantly stronger due to the EGFR-mediated endocytosis (Figure 3d,e), similar to that of A549 cell pellets. In summary, $Au_{50}Ag_2$−PEG-Ab represented an efficient contrast agent enabling targeted and sensitive PA imaging in cells, which was beneficial for subsequent *in vivo* PA imaging.

$Au_{50}Ag_2$−PEG-Ab Nanoagent for *In Vivo* 3D Multispectral PA Imaging

The *in vivo* PA imaging ability of $Au_{50}Ag_2$−PEG-Ab was first examined at subcutaneous (s.c.) locations of healthy nude mice. After the s.c. injection, the locations showed concentration-dependent PA signals (Figure S27), indicating the feasibility of the $Au_{50}Ag_2$-based nanoagent for *in vivo* imaging. With A549 xenograft tumor-bearing mice as models, the unmixed PA signals of $Au_{50}Ag_2$−PEG-Ab, DeoxyHb, and OxyHb in the tumor were monitored by 3D multispectral PA imaging after s.c. injection of $Au_{50}Ag_2$−PEG-Ab (Figures 4a and S28). The signal of $Au_{50}Ag_2$−PEG-Ab gradually increased and reached the maximum at 7 h postinjection, while the signals of endogenous DeoxyHb and OxyHb, as well as the oxygen saturation (sO_2) and total hemoglobin (HbT) that, respectively, reflect the local blood oxygenation and blood volume,[48] did not change significantly (Figure 4b,c). The variation tendency of the $Au_{50}Ag_2$−PEG-Ab signal was consistent with that of single-wavelength PA imaging at 715 nm (Figure S29). Compared to the single-wavelength PA image at 0 h, the unmixed PA image exhibited a lower background, indicating the enhanced contrast owing to the

https://doi.org/10.1021/cbmi.6c00115
Chem. Biomed. Imaging XXXX, XXX, XXX−XXX

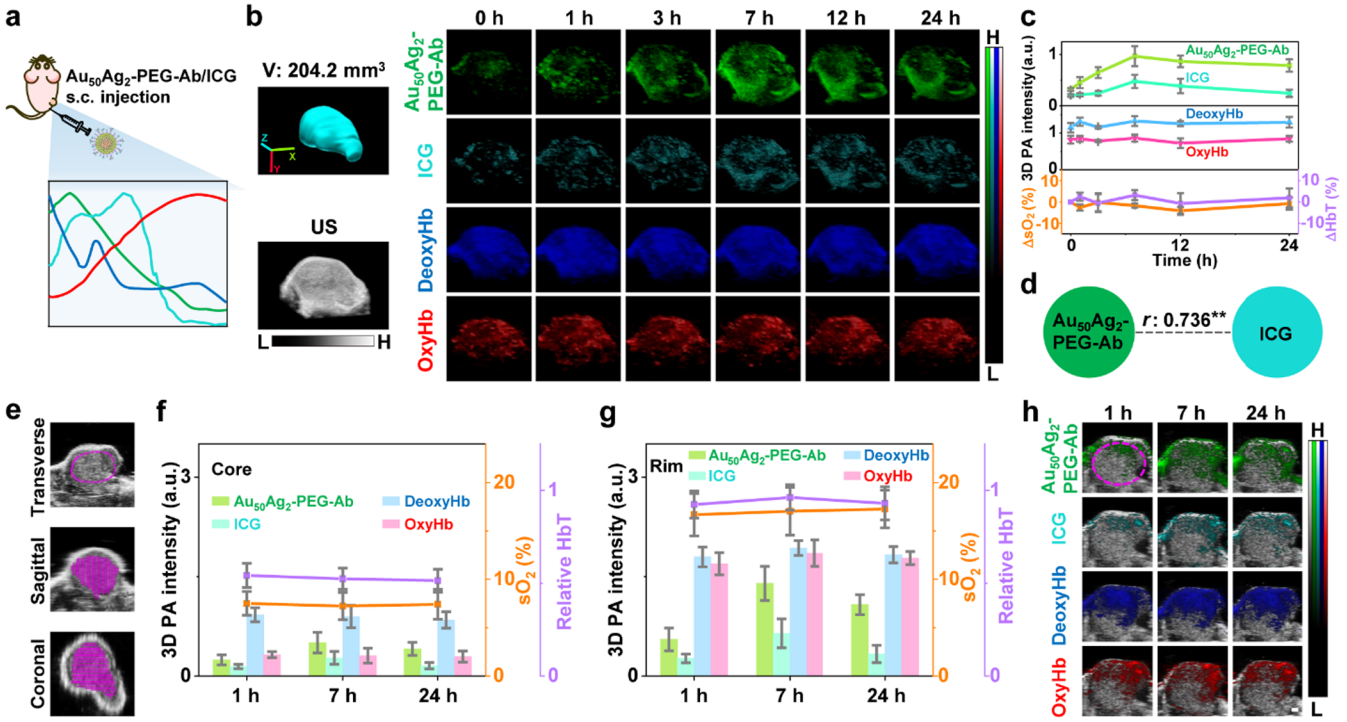

Figure 5. *In vivo* 3D multispectral PA imaging of four components in tumors upon s.c. injection. (a) PA spectra of $Au_{50}Ag_2$−PEG-Ab (green), ICG (cyan), DeoxyHb (blue), and OxyHb (red) in A549 tumor after the s.c. injection of $Au_{50}Ag_2$−PEG-Ab/ICG. (b) Representative 3D volume and US image, and multispectral PA images of the tumor before (0 h) and after the s.c. injection of $Au_{50}Ag_2$−PEG-Ab/ICG (17 μM, 100 μL) for different times. (c) 3D PA intensity of $Au_{50}Ag_2$−PEG-Ab, ICG, DeoxyHb, and OxyHb, and the relative changes of sO_2 and HbT at different times. Data are presented as mean ± SD (n = 3 mice). (d) Correlation analysis between $Au_{50}Ag_2$−PEG-Ab and ICG in 3 mice at six time points. $^{**}p < 0.001$. (e) Representative 2D transverse-, sagittal-, and coronal-view images of the 3D core regions of the $Au_{50}Ag_2$−PEG-Ab/ICG-treated tumor. (f and g) 3D PA intensity of $Au_{50}Ag_2$−PEG-Ab, ICG, DeoxyHb, and OxyHb, as well as sO_2 and HbT within the (f) core and (g) rim regions of tumors after the $Au_{50}Ag_2$−PEG-Ab/ICG treatment for 1, 7, and 24 h. Data are presented as mean ± SD (n = 3 mice). (h) Representative 2D multispectral US/PA images of the $Au_{50}Ag_2$−PEG-Ab/ICG-treated tumor at 1, 7, and 24 h. Purple dashed loop indicates the core region. Scale bar: 1 mm.

separation of endogenous DeoxyHb and OxyHb signals. Further investigations indicated that when the volume was less than ∼100 mm^3, the tumor volume did not significantly affect the PA signals of $Au_{50}Ag_2$−PEG-Ab, DeoxyHb, and OxyHb, as well as sO_2 and HbT in tumors at 7 h post s.c. injection (Figure 4d,e), although early tumor development showed growing angiogenesis,[49,50] which was presumably attributed to the fixed injected amount of nanoagent. However, with a further increase in tumor volume, these signals decreased markedly, which was due to the emergence of obvious hypoxia induction at greater tumor volume (∼100 mm^3)[51,52] and the resistance to nanoparticle penetration induced by suppressed angiogenesis and increasing interstitial fluid pressure and solid stress during tumor rapid progression.[53,54] Notably, the PA signal of DeoxyHb was stronger than that of OxyHb in tumors of all volumes, indicating the hypoxic characteristic of the tumor, and the difference between DeoxyHb and OxyHb signals increased with decreasing sO_2 when the tumor volumes exceeded 200 mm^3, similar to the previous report.[55] Pearson correlation analysis demonstrated the positive correlation between the PA signal of $Au_{50}Ag_2$−PEG-Ab and that of DeoxyHb or OxyHb (r = 0.859 or 0.829) in tumors, and also sO_2 or HbT (r = 0.732 or 0.795) (Figure 4f).

To reveal the delivery of $Au_{50}Ag_2$−PEG-Ab to solid tumors and the nanoprobe−tumor interactions, ICG-labeled $Au_{50}Ag_2$−PEG-Ab ($Au_{50}Ag_2$−PEG-Ab/ICG) was prepared, in which ICG served as an indirect indicator of the spatial distribution of $Au_{50}Ag_2$−PEG-Ab. It exhibited the same hydrodynamic diameter as $Au_{50}Ag_2$−PEG-Ab in PBS, and the characteristic absorption and fluorescence peaks of ICG at 780 and 812 nm, respectively (Figure S30). Then, the unmixed PA signals of $Au_{50}Ag_2$−PEG-Ab, ICG, DeoxyHb, and OxyHb in the tumor were monitored by 3D multispectral PA imaging after the s.c. injection of $Au_{50}Ag_2$−PEG-Ab/ICG into A549 xenograft tumor-bearing mice (Figures 5a and S31). Here, the mice with tumor volumes of ∼200 mm^3 and low hypoxic levels were used to distinguish DeoxyHb and OxyHb. As shown in Figure 5b,c, the unmixed PA signals of $Au_{50}Ag_2$−PEG-Ab and ICG showed identical variation tendency, similar to the above $Au_{50}Ag_2$−PEG-Ab-treated results (Figure 4c); meanwhile, DeoxyHb, OxyHb, sO_2, and HbT values basically remained stable. Moreover, the Pearson correlation coefficient (0.736; Figure 5d) indicated the relatively strong positive correlation between the unmixed PA signals of $Au_{50}Ag_2$−PEG-Ab and ICG, confirming their spatial colocalization. The dynamic distributions of these signals were further analyzed by manually segmenting the entire tumor into a 1 mm thick rim and the central core[50] (Figure 5e). The overall PA signals of $Au_{50}Ag_2$−PEG-Ab, ICG, DeoxyHb, and OxyHb, as well as the sO_2 and HbT values in the core region at different times postinjection were significantly lower than those in the rim region (Figure 5f−h), which could be attributed to the lower vascular density and insufficient blood supply at the central zone of tumor

https://doi.org/10.1021/cbmi.6c00115
Chem. Biomed. Imaging XXXX, XXX, XXX−XXX

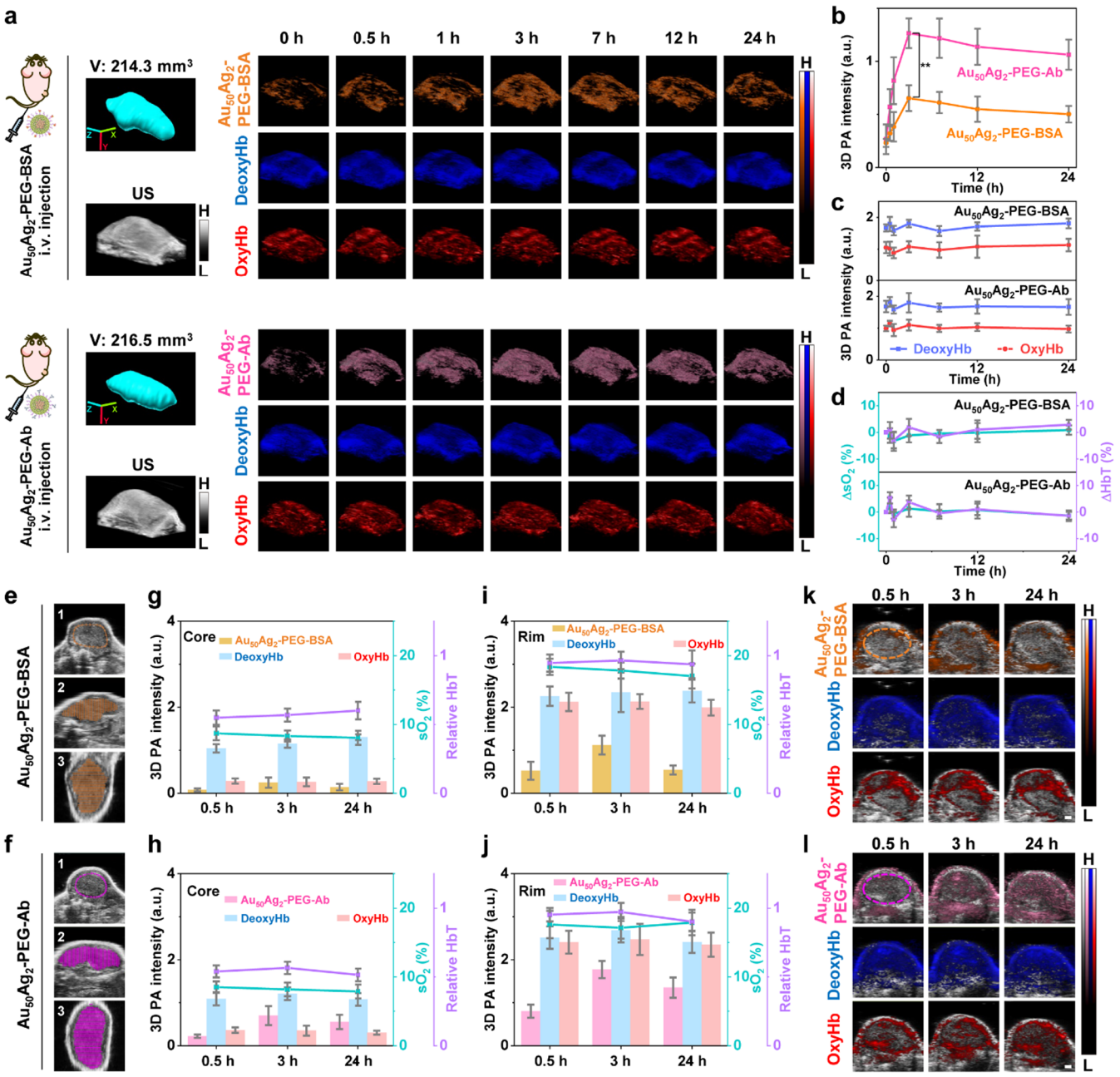

Figure 6. *In vivo* tumor-targeted 3D multispectral PA imaging after i.v. injection. (a) Representative 3D volumes and US images, and multispectral PA images of tumors in the A549 tumor-bearing mice before (0 h) and after i.v. injection of $Au_{50}Ag_2$−PEG-BSA or $Au_{50}Ag_2$−PEG-Ab (133 μM, 200 μL) for different times. (b−d) 3D PA intensity of (b) $Au_{50}Ag_2$−PEG-BSA and $Au_{50}Ag_2$−PEG-Ab, (c) DeoxyHb and OxyHb, and (d) the relative changes of sO_2 and HbT at different times. Data are presented as mean ± SD (n = 3 mice). **p = 0.0047. (e and f) Representative 2D (1) transverse-view, (2) sagittal-view, and (3) coronal-view images of the 3D core region of (e) $Au_{50}Ag_2$−PEG-BSA or (f) $Au_{50}Ag_2$−PEG-Ab treated tumor. (g−j) 3D PA intensity of $Au_{50}Ag_2$−PEG-BSA, $Au_{50}Ag_2$−PEG-Ab, DeoxyHb, and OxyHb, as well as sO_2 and HbT within the (g and h) core and (i and j) rim regions of tumors after (g and i) $Au_{50}Ag_2$−PEG-BSA or (h and j) $Au_{50}Ag_2$−PEG-Ab treatment for 0.5, 3, and 24 h. Data are presented as mean ± SD (n = 3 mice). (k and l) 2D multispectral US/PA images of (k) $Au_{50}Ag_2$−PEG-BSA-treated or (l) $Au_{50}Ag_2$−PEG-Ab-treated tumor at 0.5, 3, and 24 h. An orange or purple dashed loop indicates the core region. Scale bars: 1 mm.

compared to those at the tumor interface,[56] indicating the increasing hypoxia induction at the tumor core.[50,57] Interestingly, the levels of DeoxyHb, OxyHb, sO_2, and HbT at both the core and rim regions of the tumor remained stable in the whole observed period, while the PA signals of $Au_{50}Ag_2$−PEG-Ab and ICG decreased at 24 h postinjection due to the efflux of $Au_{50}Ag_2$−PEG-Ab/ICG from tumor tissues. The increasing PA signals of $Au_{50}Ag_2$−PEG-Ab and ICG within 7 h postinjection indicated that more $Au_{50}Ag_2$−PEG-Ab/ICG (or $Au_{50}Ag_2$−PEG-Ab) entered the core hypoxic region with high-expression EGFR. The delivery of $Au_{50}Ag_2$−PEG-Ab/ICG (or $Au_{50}Ag_2$−PEG-Ab) into the tumor could probably be interpreted as the enhanced permeability and retention effect or the active transport and retention principle.[58]

Next, the *in vivo* delivery of $Au_{50}Ag_2$−PEG-Ab was examined via the second near-infrared fluorescence (NIR-II FL) imaging after intravenous (i.v.) injection of $Au_{50}Ag_2$−PEG-Ab/ICG into A549 tumor-bearing mice. $Au_{50}Ag_2$−PEG-Ab/ICG

https://doi.org/10.1021/cbmi.6c00115
Chem. Biomed. Imaging XXXX, XXX, XXX−XXX

showed strong fluorescence from ICG at different exposure times, while the NIR-II emission of $Au_{50}Ag_2$−PEG-Ab was negligible because of the weak photoluminescence of $Au_{50}Ag_2$ (Figure S32). After injection, bright ICG fluorescence was observed throughout the body until 12 h, and the FL intensity in the tumor gradually increased and reached the maximum at 3 h (Figure S33), indicating efficient delivery and tumor accumulation of $Au_{50}Ag_2$−PEG-Ab. As for PA imaging, with $Au_{50}Ag_2$−PEG-BSA-treated mice as nontargeted controls, $Au_{50}Ag_2$−PEG-Ab-treated mice exhibited stronger PA signals in tumors after the i.v. injection (Figure 6a,b), demonstrating the Ab-mediated targeting advantage. Both the unmixed PA signals of $Au_{50}Ag_2$−PEG-BSA and $Au_{50}Ag_2$−PEG-Ab in tumors gradually increased and reached the maximum at 3 h (Figure 6b), while the PA signals of DeoxyHb and OxyHb, as well as the sO_2 and HbT for $Au_{50}Ag_2$−PEG-BSA- and $Au_{50}Ag_2$−PEG-Ab-treated mice, exhibited negligible changes (Figure 6c,d). Noticeably, the time to reach the maximum PA signal for $Au_{50}Ag_2$−PEG-Ab-treated mice by the i.v. injection (3 h) was earlier than that by the s.c. injection (7 h), which presumably resulted from the faster rate of nanoprobe entry into the bloodstream. The dynamic distributions of these signals were further analyzed by segmenting $Au_{50}Ag_2$−PEG-BSA- and $Au_{50}Ag_2$−PEG-Ab-treated tumors in the same way (Figure 6e,f). The overall PA signals of $Au_{50}Ag_2$−PEG-BSA or $Au_{50}Ag_2$−PEG-Ab, DeoxyHb, and OxyHb, as well as sO_2 and HbT in the core regions, were also significantly lower than those in rim regions at different times, and the PA intensity of $Au_{50}Ag_2$−PEG-Ab was higher than that of $Au_{50}Ag_2$−PEG-BSA in both the core and rim regions (Figure 6g−j). Moreover, the PA signals of $Au_{50}Ag_2$−PEG-BSA and $Au_{50}Ag_2$−PEG-Ab at 0.5 h were mainly localized in rim vascular regions, while stronger signals were observed in both rim vascular regions and core hypoxic regions at 3 h, and the signals decreased in both regions at 24 h due to the efflux of nanoagents from tumor tissues (Figure 6k,l), like the above subcutaneous injection results. Significantly, at 3 h, the PA signal of $Au_{50}Ag_2$−PEG-Ab was detected in almost the entire tumor region, which is markedly different from the incomplete signal distribution of $Au_{50}Ag_2$−PEG-BSA. This indicated that the relatively complete tissue infiltration of $Au_{50}Ag_2$−PEG-Ab via the target-mediated pathway, which further led to the observable PA signal of $Au_{50}Ag_2$−PEG-Ab in both the core and rim regions at 24 h. In addition, hematoxylin and eosin staining images of major organs from PBS and $Au_{50}Ag_2$−PEG-Ab-treated mice did not show significant damage after i.v. injection for 2 weeks (Figure S34), demonstrating the long-term *in vivo* biosafety of $Au_{50}Ag_2$-based nanoagents.

CONCLUSION

This work develops an atomically precise $Au_{50}Ag_2$-based nanoagent through the dimerization and engineering of Au_{25} nanoclusters for *in vivo* 3D multispectral PA imaging in tumors. This dimerization leads to a distinct red-shift from 680 to 710 nm in the PA spectrum, a 5.1-fold enhancement in PA sensitivity, and an increase in PCE from 33.9% to 47.1%. Given the superior PA performance of the dimeric $Au_{50}Ag_2$, a hydrophobic-to-hydrophilic transfer is implemented to construct $Au_{50}Ag_2$−PEG via encapsulation with amphiphilic phospholipids. This transformation results in an increased PCE of up to 54.7%, improved photothermal stability, a red-shifted characteristic PA peak in the NIR region, and an invariant PA sensitivity. $Au_{50}Ag_2$−PEG demonstrates superior PA stability under 5360 laser pulses, remarkable storage stability in physiological media, and versatile bioconjugation capability for targeted applications. With an anti-EGFR antibody as a model conjugate, the $Au_{50}Ag_2$−PEG-Ab nanoagent enables cellular PA quantitation by generating intense PA contrast in target tumor cell pellets and specific 3D multispectral PA imaging of multiple chromophores (e.g., $Au_{50}Ag_2$−PEG-Ab, DeoxyHb, OxyHb, ICG) within solid tumors of tumor-bearing mice after systemic administration. PA imaging with this nanoagent unveils *in vivo* spatiotemporal heterogeneities of tumor-associated events, such as blood oxygenation, blood volume, and nanoprobe delivery, which provides unique insights into the interactions between the nanoagents and solid tumors.

To our knowledge, this work presents the first case of an atomic-precision metal nanocluster engineered for *in vivo* multispectral PA imaging, establishing a generalizable paradigm for constructing high-performance PA contrast agents. Compared to conventional PA nanoagents, for example, carbon nanomaterials[59] and gold nanocrystals,[15] this nanocluster-based nanoagent integrates superior properties of characteristic NIR absorption, a strong PA response, and robust photostability, enabling high-fidelity *in vivo* multispectral imaging. The integration of spectral resolution, 3D imaging technique, and targeting specificity further improves the imaging precision. This programmable agent can be readily adapted to diverse diseases by changing the recognition modules. Given the relatively limited tissue penetration depth of a 715 nm laser, this nanoagent could be particularly well suited for the superficial diseases, for example, obesity.[60] To extend its imaging utility to deep-seated pathological conditions, such as gastric cancer[61] or ischemic stroke,[62] future studies will focus on the development of structural engineered nanoclusters with higher molar extinction coefficients and broader spectral tunability, especially in the second NIR region. Nevertheless, we acknowledge the limited sample size in the current *in vivo* study, and subsequent preclinical trials with larger cohorts are warranted to enable more robust statistical analyses and to further corroborate the clinical translational potential of this platform. Furthermore, a comprehensive assessment of the long-term biocompatibility and metabolic fate of the nanocluster-based agent will consolidate its foundation for clinical translation.

ASSOCIATED CONTENT

Supporting Information

The Supporting Information is available free of charge at https://pubs.acs.org/doi/10.1021/cbmi.6c00115.

Materials and methods, supplementary figures (additional characterizations of nanoclusters, optimization of aqueous-phase synthesis conditions, synthesis characterizations and optical properties of aqueous-phase nanoagents, cytotoxicity, intracellular endocytosis and colocalization analysis, PA imaging in cell pellets and subcutaneous locations of mice, workflow of image acquisition and data processing for 3D multispectral PA imaging, NIR-II fluorescence imaging of mice, and hematoxylin and eosin staining images), supplementary tables (comparison of PCE with photothermal nanoclusters and nanocluster-based agents), and supplementary references (PDF)

https://doi.org/10.1021/cbmi.6c00115
Chem. Biomed. Imaging XXXX, XXX, XXX−XXX

AUTHOR INFORMATION

Corresponding Authors

Yan Zhu − *State Key Laboratory of Coordination Chemistry, Key Laboratory of Mesoscopic Chemistry of Ministry of Education, School of Chemistry, Nanjing University, Nanjing 210023, China;* orcid.org/0000-0002-5993-4110; Email: zhuyan@nju.edu.cn

Huangxian Ju − *State Key Laboratory of Analytical Chemistry for Life Science, School of Chemistry, Nanjing University, Nanjing 210023, China;* orcid.org/0000-0002-6741-5302; Email: hxju@nju.edu.cn

Authors

Ying An − *State Key Laboratory of Analytical Chemistry for Life Science, School of Chemistry, Nanjing University, Nanjing 210023, China*

Xu Liu − *State Key Laboratory of Coordination Chemistry, Key Laboratory of Mesoscopic Chemistry of Ministry of Education, School of Chemistry, Nanjing University, Nanjing 210023, China;* orcid.org/0000-0003-0668-5074

Yiran Li − *State Key Laboratory of Analytical Chemistry for Life Science, School of Chemistry, Nanjing University, Nanjing 210023, China*

Kun Wu − *State Key Laboratory of Analytical Chemistry for Life Science, School of Chemistry, Nanjing University, Nanjing 210023, China*

Hao Wang − *State Key Laboratory of Coordination Chemistry, Key Laboratory of Mesoscopic Chemistry of Ministry of Education, School of Chemistry, Nanjing University, Nanjing 210023, China*

Kaiyu Zhang − *State Key Laboratory of Analytical Chemistry for Life Science, School of Chemistry, Nanjing University, Nanjing 210023, China*

Jing Jia − *State Key Laboratory of Analytical Chemistry for Life Science, School of Chemistry, Nanjing University, Nanjing 210023, China*

Chaoyi Yang − *State Key Laboratory of Analytical Chemistry for Life Science, School of Chemistry, Nanjing University, Nanjing 210023, China*

Yunlong Chen − *State Key Laboratory of Analytical Chemistry for Life Science, School of Chemistry, Nanjing University, Nanjing 210023, China;* orcid.org/0000-0002-3775-3028

Complete contact information is available at: https://pubs.acs.org/10.1021/cbmi.6c00115

Author Contributions

[§]Y.A. and X.L. contributed equally to this work.

Notes

The authors declare no competing financial interest.

ACKNOWLEDGMENTS

This research was supported by the National Natural Science Foundation of China (21890741, 21827812, 22125202, 22101128, and 22575104). We thank Dr. Yunfeng Zhao and Shanshan Wang of FUJIFILM Co., Ltd. for PA imaging technical support and Prof. Deju Ye of Nanjing University for the photothermal device support.

REFERENCES

(1) Taruttis, A.; Ntziachristos, V. Advances in Real-Time Multispectral Optoacoustic Imaging and Its Applications. *Nat. Photonics* **2015**, *9*, 219−227.

(2) Steinberg, I.; Huland, D. M.; Vermesh, O.; Frostig, H. E.; Tummers, W. S.; Gambhir, S. S. Photoacoustic Clinical Imaging. *Photoacoustics* **2019**, *14*, 77−98.

(3) Wang, L. V.; Yao, J. A Practical Guide to Photoacoustic Tomography in the Life Sciences. *Nat. Methods* **2016**, *13*, 627−638.

(4) Jo, J.; Lee, C. H.; Kopelman, R.; Wang, X. In Vivo Quantitative Imaging of Tumor pH by Nanosonophore Assisted Multispectral Photoacoustic Imaging. *Nat. Commun.* **2017**, *8*, No. 471.

(5) Wood, C. A.; Han, S.; Kim, C. S.; Wen, Y.; Sampaio, D. R. T.; Harris, J. T.; Homan, K. A.; Swain, J. L.; Emelianov, S. Y.; Sood, A. K.; Cook, J. R.; Sokolov, K. V.; Bouchard, R. R. Clinically Translatable Quantitative Molecular Photoacoustic Imaging with Liposome-Encapsulated ICG J-Aggregates. *Nat. Commun.* **2021**, *12*, No. 5410.

(6) Lei, S.; Zhang, J.; Blum, N. T.; Li, M.; Zhang, D.-Y.; Yin, W.; Zhao, F.; Lin, J.; Huang, P. In Vivo Three-Dimensional Multispectral Photoacoustic Imaging of Dual Enzyme-Driven Cyclic Cascade Reaction for Tumor Catalytic Therapy. *Nat. Commun.* **2022**, *13*, No. 1298.

(7) Attia, A. B. E.; Balasundaram, G.; Moothanchery, M.; Dinish, U. S.; Bi, R.; Ntziachristos, V.; Olivo, M. A Review of Clinical Photoacoustic Imaging: Current and Future Trends. *Photoacoustics* **2019**, *16*, No. 100144.

(8) Ma, Y.; Shang, J.; Liu, L.; Li, M.; Xu, X.; Cao, H.; Xu, L.; Sun, W.; Song, G.; Zhang, X.-B. Rational Design of a Double-Locked Photoacoustic Probe for Precise In Vivo Imaging of Cathepsin B in Atherosclerotic Plaques. *J. Am. Chem. Soc.* **2023**, *145*, 17881−17891.

(9) Weber, J.; Beard, P. C.; Bohndiek, S. E. Contrast Agents for Molecular Photoacoustic Imaging. *Nat. Methods* **2016**, *13*, 639−650.

(10) Wu, Y.; Zeng, F.; Zhao, Y.; Wu, S. Emerging Contrast Agents for Multispectral Optoacoustic Imaging and Their Biomedical Applications. *Chem. Soc. Rev.* **2021**, *50*, 7924−7940.

(11) Wang, S.; Zhang, L.; Zhao, J.; He, M.; Huang, Y.; Zhao, S. A Tumor Microenvironment−Induced Absorption Red-Shifted Polymer Nanoparticle for Simultaneously Activated Photoacoustic Imaging and Photothermal Therapy. *Sci. Adv.* **2021**, *7*, No. eabe3588.

(12) Zhang, C.; Wu, Y.; Zeng, F.; Wen, Y.; Chen, J.; Deng, G.; Zhang, L.; Zhao, S.; Wu, S.; Zhao, Y. Structurally Modulated Formation of Cyanine J-Aggregates with Sharp and Tunable Spectra for Multiplexed Optoacoustic and Fluorescence Bioimaging. *Angew. Chem., Int. Ed.* **2024**, *63*, No. e202406694.

(13) Jokerst, J. V.; Thangaraj, M.; Kempen, P. J.; Sinclair, R.; Gambhir, S. S. Photoacoustic Imaging of Mesenchymal Stem Cells in Living Mice via Silica-Coated Gold Nanorods. *ACS Nano* **2012**, *6*, 5920−5930.

(14) Fu, Q.; Zhu, R.; Song, J.; Yang, H.; Chen, X. Photoacoustic Imaging: Contrast Agents and Their Biomedical Applications. *Adv. Mater.* **2019**, *31*, No. 1805875.

(15) Chen, Y.-S.; Zhao, Y.; Yoon, S. J.; Gambhir, S. S.; Emelianov, S. Miniature Gold Nanorods for Photoacoustic Molecular Imaging in the Second Near-Infrared Optical Window. *Nat. Nanotechnol.* **2019**, *14*, 465−472.

(16) Wang, X.; Ji, S.; Zhu, M.; Yao, Q.; Xie, J. Chiral Metal Nanoclusters: Structure, Synthesis, and Optoelectronic Applications. *Aggregate* **2026**, *7*, No. e70313.

(17) Yang, Z.; Yi, Y.; Wang, Y.; Ye, Y.; Zhang, R.; Ma, G.; Chen, T.; Xu, W. W.; Xie, J. Assembly of Tetrahedral Units in the Atomic-Resolved Structural Evolution of Gold Nanostructures. *J. Am. Chem. Soc.* **2026**, *148*, 10848−10858.

(18) Shi, W.-Q.; Zeng, L.; He, R.-L.; Han, X.-S.; Guan, Z.-J.; Zhou, M.; Wang, Q.-M. Near-Unity NIR Phosphorescent Quantum Yield from a Room-Temperature Solvated Metal Nanocluster. *Science* **2024**, *383*, 326−330.

(19) Zhou, M.; Higaki, T.; Li, Y.; Zeng, C.; Li, Q.; Sfeir, M. Y.; Jin, R. Three-Stage Evolution from Nonscalable to Scalable Optical

Properties of Thiolate-Protected Gold Nanoclusters. *J. Am. Chem. Soc.* **2019**, *141*, 19754−19764.
(20) Luo, L.; Liu, Z.; Kong, J.; Gianopoulos, C. G.; Coburn, I.; Kirschbaum, K.; Zhou, M.; Jin, R. Three-Atom-Wide Gold Quantum Rods with Periodic Elongation and Strongly Polarized Excitons. *Proc. Natl. Acad. Sci. U.S.A.* **2024**, *121*, No. e2318537121.
(21) Xu, W.; Feng, R.; Xu, S.; Wang, L. Enzyme Catalysis Induced Nanocluster Assembly into Micrometer-Size Monolayered Nanosheets with Enhanced Near-Infrared Region II Emission. *J. Am. Chem. Soc.* **2026**, *148*, 14855−14865.
(22) Baghdasaryan, A.; Liu, H.; Ren, F.; Hsu, R.; Jiang, Y.; Wang, F.; Zhang, M.; Grigoryan, L.; Dai, H. Intratumor Injected Gold Molecular Clusters for NIR-II Imaging and Cancer Therapy. *Proc. Natl. Acad. Sci. U.S.A.* **2024**, *121*, No. e2318265121.
(23) Sharma, N.; Mohammad, W.; Guével, X. L.; Shanavas, A. Gold Nanoclusters as High Resolution NIR-II Theranostic Agents. *Chem. Biomed. Imaging* **2024**, *2*, 462−480.
(24) Song, X.; Wei, J.; Cai, X.; Liu, Y.; Wu, F.; Tong, S.; Li, S.; Yao, Q.; Xie, J.; Yang, H. Organotropic Engineering of Luminescent Gold Nanoclusters for In Vivo Imaging of Lung Orthotopic Tumors. *ACS Nano* **2024**, *18*, 33555−33565.
(25) Varnavski, O.; Ramakrishna, G.; Kim, J.; Lee, D.; Goodson III, T. Optically Excited Acoustic Vibrations in Quantum-Sized Monolayer-Protected Gold Clusters. *ACS Nano* **2010**, *4*, 3406−3412.
(26) Jiang, X.; Du, B.; Tang, S.; Hsieh, J.-T.; Zheng, J. Photoacoustic Imaging of Nanoparticle Transport in the Kidneys at High Temporal Resolution. *Angew. Chem., Int. Ed.* **2019**, *58*, 5994−6000.
(27) Shen, D.; Henry, M.; Trouillet, V.; Comby-Zerbino, C.; Bertorelle, F.; Sancey, L.; Antoine, R.; Coll, J.-L.; Josserand, V.; Guével, X. L. Zwitterion Functionalized Gold Nanoclusters for Multimodal Near Infrared Fluorescence and Photoacoustic Imaging. *APL Mater.* **2017**, *5*, No. 053404.
(28) Rad, A. T.; Bao, Y.; Jang, H.-S.; Xia, Y.; Sharma, H.; Dormidontova, E. E.; Zhao, J.; Arora, J.; John, V. T.; Tang, B. Z.; Dainese, T.; Hariri, A.; Jokerst, J. V.; Maran, F.; Nieh, M.-P. Aggregation-Enhanced Photoluminescence and Photoacoustics of Atomically Precise Gold Nanoclusters in Lipid Nanodiscs ($NANO^2$). *Adv. Funct. Mater.* **2021**, *31*, No. 2009750.
(29) Zhou, C.; Wang, M.; Yao, Q.; Zhou, Y.; Hou, C.; Xia, J.; Wang, Z.; Chen, J.; Xie, J. Ligand-Dependent Aggregation-Enhanced Photoacoustic of Atomically Precise Metal Nanocluster. *Aggregate* **2024**, *5*, No. e401.
(30) Liu, X.; Saranya, G.; Huang, X.; Cheng, X.; Wang, R.; Chen, M.; Zhang, C.; Li, T.; Zhu, Y. $Ag_2Au_{50}(PET)_{36}$ Nanocluster: Dimeric Assembly of $Au_{25}(PET)_{18}$ Enabled by Silver Atoms. *Angew. Chem., Int. Ed.* **2020**, *59*, 13941−13946.
(31) Li, N.-L.; Wei, J.; Ran, X.-Y.; Li, J.; Shen, L.; Zhang, F.; Dai, Q.; Wang, W.; Li, K.; Wan, X.-K. All-Alkynyl Protected Rod-Shaped $Au_9(AgCu)_{126}$ Nanocluster with Remarkable Photothermal Conversion. *Angew. Chem., Int. Ed.* **2025**, *64*, No. e202503036.
(32) Wang, Z.; Zhu, Y.-J.; Ahlstedt, O.; Konstantinou, K.; Akola, J.; Tung, C.-H.; Alkan, F.; Sun, D. Three in One: Three Different Molybdates Trapped in a Thiacalix[4]arene Protected Ag_{72} Nanocluster for Structural Transformation and Photothermal Conversion. *Angew. Chem., Int. Ed.* **2024**, *63*, No. e202314515.
(33) Fang, L.; Fan, W.; Bian, G.; Wang, R.; You, Q.; Gu, W.; Xia, N.; Liao, L.; Li, J.; Deng, H.; Yan, N.; Wu, Z. Sandwich-Kernelled AgCu Nanoclusters with Golden Ratio Geometry and Promising Photothermal Efficiency. *Angew. Chem., Int. Ed.* **2023**, *62*, No. e202305604.
(34) You, Q.; Jiang, X.-L.; Fan, W.; Cui, Y.-S.; Zhao, Y.; Zhuang, S.; Gu, W.; Liao, L.; Xu, C.-Q.; Li, J.; Wu, Z. Pd_8 Nanocluster with Nonmetal-to-Metal-Ring Coordination and Promising Photothermal Conversion Efficiency. *Angew. Chem., Int. Ed.* **2024**, *63*, No. e202313491.
(35) Wang, Z.; Wang, Y.; Zhang, C.; Zhu, Y.-J.; Song, K.-P.; Aikens, C. M.; Tung, C.-H.; Sun, D. Silvery Fullerene in Ag_{102} Nanosaucer. *Natl. Sci. Rev.* **2024**, *11*, No. nwae192.
(36) Chen, J.; Gu, P.; Ran, G.; Zhang, Y.; Li, M.; Chen, B.; Lu, H.; Han, Y.-Z.; Zhang, W.; Tang, Z.; Yan, Q.; Sun, R.; Fu, X.; Chen, G.; Shi, Z.; Wang, S.; Liu, X.; Li, J.; Wang, L.; Zhu, Y.; Shen, J.; Tang, B. Z.; Fan, C. Atomically Precise Photothermal Nanomachines. *Nat. Mater.* **2024**, *23*, 271−280.
(37) Gutierrez, N. M. C.; Clainche, T. L.; Bulin, A.-L.; Leo, S.; Kadri, M.; Abdelhamid, A. G. A.; Pujol-Solé, N.; Obaid, G.; Hograindleur, M.-A.; Gardette, V.; Busser, B.; Motto-Ros, V.; Josserand, V.; Henry, M.; Sancey, L.; Hurbin, A.; Elleaume, H.; Kandiah, E.; Guével, X. L.; Coll, J.-L.; Broekgaarden, M. Engineering Radiocatalytic Nanoliposomes with Hydrophobic Gold Nanoclusters for Radiotherapy Enhancement. *Adv. Mater.* **2024**, *36*, No. 2404605.
(38) Al Zaki, A.; Joh, D.; Cheng, Z.; Barros, A. L. B. D.; Kao, G.; Dorsey, J.; Tsourkas, A. Gold-Loaded Polymeric Micelles for Computed Tomography-Guided Radiation Therapy Treatment and Radiosensitization. *ACS Nano* **2014**, *8*, 104−112.
(39) Link, S.; Burda, C.; Mohamed, M. B.; Nikoobakht, B.; El-Sayed, M. A. Laser Photothermal Melting and Fragmentation of Gold Nanorods: Energy and Laser Pulse-Width Dependence. *J. Phys. Chem. A* **1999**, *103*, 1165−1170.
(40) Link, S.; Burda, C.; Nikoobakht, B.; El-Sayed, M. A. Laser-Induced Shape Changes of Colloidal Gold Nanorods Using Femtosecond and Nanosecond Laser Pulses. *J. Phys. Chem. B* **2000**, *104*, 6152−6163.
(41) González-Rubio, G.; Guerrero-Martínez, A.; Liz-Marzán, L. M. Reshaping, Fragmentation, and Assembly of Gold Nanoparticles Assisted by Pulse Lasers. *Acc. Chem. Res.* **2016**, *49*, 678−686.
(42) Aldonza, M. B. D.; Ku, J.; Hong, J.-Y.; Kim, D.; Yu, S. J.; Lee, M.-S.; Prayogo, M. C.; Tan, S.; Kim, D.; Han, J.; Lee, S. K.; Im, S. G.; Ryu, H. S.; Kim, Y. Prior Acquired Resistance to Paclitaxel Relays Diverse EGFR-Targeted Therapy Persistence Mechanisms. *Sci. Adv.* **2020**, *6*, No. eaav7416.
(43) Shao, C.; Tang, B.; Chu, J. C. H.; Lau, K. M.; Wong, W.-T.; Che, C.-M.; Tai, W. C. S.; Wong, W.-T.; Wong, C. T. T. Macrophage-Engaging Peptidic Bispecific Antibodies (pBsAbs) for Immunotherapy via a Facile Bioconjugation Strategy. *Chem. Sci.* **2024**, *15*, 11272−11278.
(44) Ahmad, S.; Barashkin, A. A.; Jadidi, H.; Calderon, A.; Amadou, H.; Ornberg, A. B., Jr.; Nesterov, E. E.; Nesterova, I. V. Novel "C-Clamp" Design of Highly Selective Small-Molecule Sensors for Kinase Proteins. *Chem. Biomed. Imaging* **2026**, *4*, 658−668.
(45) Lei, Q.; Zhou, X.; Li, Y.; Zhao, S.; Yang, N.; Xiao, Z.; Song, C.; Yu, Q.; Deng, H. Image-Based Phenotypic Profiling Enables Rapid and Accurate Assessment of EGFR-Activating Mutations in Tissues from Lung Cancer Patients. *J. Am. Chem. Soc.* **2025**, *147*, 4552−4570.
(46) Wu, C.; Wu, K.-J.; Liu, J.-B.; Wang, W.; Leung, C.-H.; Ma, D.-L. Structure-Guided Discovery of a Luminescent Theranostic Toolkit for Living Cancer Cells and the Imaging Behavior Effect. *Chem. Sci.* **2020**, *11*, 11404−11412.
(47) Yu, S.; Hu, X.; Pan, J.; Lei, J.; Ju, H. Nanoconfined Cathodic Electrochemiluminescence for Self-Sensitized Bioimaging of Membrane Protein. *Anal. Chem.* **2023**, *95*, 16593−16599.
(48) Na, S.; Russin, J. J.; Lin, L.; Yuan, X.; Hu, P.; Jann, K. B.; Yan, L.; Maslov, K.; Shi, J.; Wang, D. J.; Liu, C. Y.; Wang, L. V. Massively Parallel Functional Photoacoustic Computed Tomography of the Human Brain. *Nat. Biomed. Eng.* **2022**, *6*, 584−592.
(49) Zhou, H.-C.; Chen, N.; Zhao, H.; Yin, T.; Zhang, J.; Zheng, W.; Song, L.; Liu, C.; Zheng, R. Optical-Resolution Photoacoustic Microscopy for Monitoring Vascular Normalization during Anti-Angiogenic Therapy. *Photoacoustics* **2019**, *15*, No. 100143.
(50) Kim, J.; Lee, J.; Choi, S.; Lee, H.; Yang, J.; Jeon, H.; Sung, M.; Kim, W. J.; Kim, C. 3D Multiparametric Photoacoustic Computed Tomography of Primary and Metastatic Tumors in Living Mice. *ACS Nano* **2024**, *18*, 18176−18190.
(51) Chen, Z.; Han, F.; Du, Y.; Shi, H.; Zhou, W. Hypoxic Microenvironment in Cancer: Molecular Mechanisms and Therapeutic Interventions. *Signal Transduction Targeted Ther.* **2023**, *8*, No. 70.
(52) Wu, X.; Xing, F.; Yang, Y.; Liu, X.; Kim, G.; Jiang, Q.; Xu, Y.; Hu, J.-J.; Liang, G.; Yoon, J. Caged Ligand-Decorated Near-Infrared Photosensitizer with In Vivo Albumin-Hijacking Capacity for Tumor-

https://doi.org/10.1021/cbmi.6c00115
Chem. Biomed. Imaging XXXX, XXX, XXX−XXX

Targeted Hypoxia-Tolerant Photoimmunotherapy of Cancer. *J. Am. Chem. Soc.* **2026**, *148*, 6135−6147.
(53) Stylianopoulos, T.; Martin, J. D.; Chauhan, V. P.; Jain, S. R.; Diop-Frimpong, B.; Bardeesy, N.; Smith, B. L.; Ferrone, C. R.; Hornicek, F. J.; Boucher, Y.; Munn, L. L.; Jain, R. K. Causes, Consequences, and Remedies for Growth-Induced Solid Stress in Murine and Human Tumors. *Proc. Natl. Acad. Sci. U.S.A.* **2012**, *109*, 15101−15108.
(54) Nakamura, Y.; Mochida, A.; Choyke, P. L.; Kobayashi, H. Nanodrug Delivery: is the Enhanced Permeability and Retention Effect Sufficient for Curing Cancer. *Bioconjugate Chem.* **2016**, *27*, 2225−2238.
(55) Xu, Q.; Pan, Y.; Liu, X.; Gao, Y.; Luan, X.; Zeng, F.; Zhou, D.; Long, W.; Wang, Y.; Song, Y. Hypoxia-Responsive Platinum Supernanoparticles for Urinary Microfluidic Monitoring of Tumors. *Angew. Chem., Int. Ed.* **2022**, *61*, No. e202114239.
(56) Wilhelm, S.; Tavares, A. J.; Dai, Q.; Ohta, S.; Audet, J.; Dvorak, H. F.; Chan, W. C. W. Analysis of Nanoparticle Delivery to Tumours. *Nat. Rev. Mater.* **2016**, *1*, No. 16014.
(57) Minchinton, A. I.; Tannock, I. F. Drug Penetration in Solid Tumours. *Nat. Rev. Cancer* **2006**, *6*, 583−592.
(58) Nguyen, L. N. M.; Ngo, W.; Lin, Z. P.; Sindhwani, S.; MacMillan, P.; Mladjenovic, S. M.; Chan, W. C. W. The Mechanisms of Nanoparticle Delivery to Solid Tumours. *Nat. Rev. Bioeng.* **2024**, *2*, 201−213.
(59) De La Zerda, A.; Zavaleta, C.; Keren, S.; Vaithilingam, S.; Bodapati, S.; Liu, Z.; Levi, J.; Smith, B. R.; Ma, T.-J.; Oralkan, O.; Cheng, Z.; Chen, X.; Dai, H.; Khuri-Yakub, B. T.; Gambhir, S. S. Carbon Nanotubes as Photoacoustic Molecular Imaging Agents in Living Mice. *Nat. Nanotechnol.* **2008**, *3*, 557−562.
(60) Chen, R.; Huang, S.; Lin, T.; Ma, H.; Shan, W.; Duan, F.; Lv, J.; Zhang, J.; Ren, L.; Nie, L. Photoacoustic Molecular Imaging-Escorted Adipose Photodynamic-Browning Synergy for Fighting Obesity with Virus-Like Complexes. *Nat. Nanotechnol.* **2021**, *16*, 455−465.
(61) Bu, F.; Shen, X.; Zhan, H.; Wang, D.; Min, L.; Song, Y.; Wang, S. Efficient Metabolomics Profiling from Plasma Extracellular Vesicles Enables Accurate Diagnosis of Early Gastric Cancer. *J. Am. Chem. Soc.* **2025**, *147*, 8672−8686.
(62) Shichita, T.; Ooboshi, H.; Yoshimura, A. Neuroimmune Mechanisms and Therapies Mediating Post-Ischaemic Brain Injury and Repair. *Nat. Rev. Neurosci.* **2023**, *24*, 299−312.

https://doi.org/10.1021/cbmi.6c00115
Chem. Biomed. Imaging XXXX, XXX, XXX−XXX